Journal of Nuclear Medicine, published on February 14, 2020 as doi:10.2967/jnumed.119.235515

Data-driven motion detection and event-by-event correction for brain PET: Comparison with Vicra

Yihuan Lu, Mika Naganawa, Takuya Toyonaga, Jean-Dominique Gallezot, Kathryn Fontaine, Silin Ren, Enette Mae Revilla, Tim Mulnix and Richard E. Carson

Department of Radiology and Biomedical Imaging, Yale University, New Haven, CT, USA

Funding sources and disclosures:

This work is funded by NIH grants R01AG052560, R01NS094253 and R03EB027209. No potential conflicts of interest relevant to this article exist.

First author and correspondence contact: Yihuan Lu, Ph.D., Department of Radiology and Biomedical Imaging, Yale University, PO Box 208048, New Haven, CT, United States, 06520-8048. E-mail: yihuan.lu@yale.edu. Phone: 2037371214.

ABSTRACT

Head motion degrades image quality and causes erroneous parameter estimates in tracer kinetic modeling in brain PET studies. Existing motion correction methods include frame-based image-registration (FIR) and correction using real-time hardware-based motion tracking (HMT) information. However, FIR cannot correct for motion within one predefined scan period while HMT is not readily available in the clinic since it typically requires attaching a tracking device to the patient. In this study, we propose a motion correction framework with a data-driven algorithm, i.e., using the PET raw data itself, to address these limitations.

Methods: We propose a data-driven algorithm, Centroid of Distribution (COD), to detect head motion. In COD, the central coordinates of the line of response (LOR) of all events are averaged over 1-sec intervals to generate a COD trace. A point-to-point change in the COD trace in one direction that exceeded a user-defined threshold was defined as a time point of head motion, which was followed by manually adding additional motion time points. All the frames defined by such time points were reconstructed without attenuation correction and rigidly registered to a reference frame. The resulting transformation matrices were then used to perform the final motion compensated reconstruction. We applied the new COD framework to 23 human dynamic datasets, all containing large head motions, with ^{18}F-FDG (N=13) and ^{11}C-UCB-J (N=10), and compared its performance with FIR and with HMT using the Vicra, which can be considered as the "gold standard".

Results: The COD method yielded 1.0±3.2% (mean ± standard deviation across all subjects and 12 grey matter regions) SUV difference for ^{18}F-FDG (3.7±5.4% for ^{11}C-UCB-J) compared to HMT while no motion correction (NMC) and FIR yielded -15.7±12.2% (-20.5±15.8%) and -4.7±6.9% (-6.2±11.0%), respectively. For ^{18}F-FDG dynamic studies, COD yielded differences of 3.6±10.9% in K_i value as compared to HMT, while NMC and FIR yielded -18.0±39.2% and -2.6±19.8%, respectively. For ^{11}C-UCB-J, COD yielded 3.7±5.2% differences in V_T compared to HMT, while NMC and FIR yielded -20.0±12.5% and -5.3±9.4%, respectively. **Conclusion:** The proposed COD-based data-driven motion correction method outperformed FIR and achieved comparable or even better performance as compared to the Vicra HMT method in both static and dynamic studies.

Key words: PET, data-driven, motion detection, motion correction, event-by-event

INTRODUCTION

The spatial resolution of PET scanners has improved over the years. For instance, the dedicated brain scanner, high resolution research tomography (HRRT), has a resolution of < 3 mm in full-width-half-maximum (FWHM). However, head motion during brain PET studies reduces image resolution (sharpness), lowers concentrations in high-uptake regions and causes bias in tracer kinetic modeling. Existing motion correction (MC) methods include frame-based image-registration (FIR) (*1*) and correction using real-time hardware motion tracking (HMT) information (*2*). FIR cannot correct for motion within one scan period (intra-frame) while HMT is not routinely used in the clinic, since it typically requires attaching a tracking device to the patient. Thus, there is a need to develop a robust data-driven approach to detect and correct head motion.

Several data-driven approaches (*3-5*) have been proposed. Thielemans et al. (*3*) used principal component analysis (PCA) and Schleyer et al. (*6*) compared PCA to an approach that used total-count changes with the aid of time-of-flight (TOF) information. However, for the real patient studies in (*3,6*), there lacked a comparison with a "gold standard". In addition, the impact of MC on accuracy of absolute quantification was not investigated in (*3,6*). Feng et al. (*5*) proposed to directly estimate the head motion using the second moment information with thorough validation study remained to be performed. Please see additional articles (*7,8*) for a more complete review.

Here, we propose a data-driven algorithm, Centroid of Distribution (COD), to detect head motion, and perform MC within the list-mode reconstruction. A similar concept had been previously proposed by other groups (*9*) and the COD method was also previously developed for respiratory motion detection (*10*) and voluntary body motion detection (*11*) with the aid of TOF information. In this paper, we extended the use of COD to a non-TOF scanner, HRRT, to detect head motion, followed by event-by-event correction (*12*). The proposed approach was compared to FIR and HMT with the Vicra, an optical HMT device (*13*)(*14*). Vicra-based correction provided continuous head motion monitoring with event-by-event MC, which can be considered as the "gold standard". The proposed method was evaluated using both SUV and model-based quantification measures for 23 human dynamic scans, all containing large head motions, with ^{18}F-FDG and ^{11}C-UCB-J (*15*).

MATERIALS AND METHODS

Human Subjects and Data Acquisitions

Twenty-three previously acquired human PET dynamic studies with 2 different radiotracers were analyzed. The subjects belonged to multiple diagnostic categories. These included thirteen with ^{18}F-FDG (injected activity: 184±4 MBq) and ten with ^{11}C-UCB-J (363±178 MBq), a novel radiotracer that binds to the synaptic vesicle glycoprotein 2A (SV2A) (*15*), which has shown its potential as a synaptic density marker in Alzheimer's disease (*16*). The 23 datasets for this study were chosen by identifying the subjects who exhibited largest head motions out of 290 examined cases. The head motion magnitude of any point within the field-of-view (FOV) was determined from the Vicra data as twice the standard deviation of motion of that point. To describe the motion of the entire brain, eight points were selected as the vertices of a 10-cm side-length cube centered in the scanner FOV. The final motion magnitude was the average of the values from the eight points. More details can be found in (*13*). This study was approved by the Yale University Human Investigation Committee and Radiation Safety Committee.

A transmission scan, used for attenuation correction, was performed before the PET emission acquisition. For both tracers, dynamic scans of 90 min duration were performed on the HRRT scanner with the Vicra used for motion monitoring. Individual T1-weighted MR images were segmented using FreeSurfer (*17*) to generate regions of interest (ROIs), which were resliced to the individual PET space based on the MR-PET rigid registration using mutual information.

COD Motion Detection and Event-by-event Motion Correction

Head motion information was extracted from the listmode data using the COD algorithm. In COD, for every listmode event i, the line-of-response (LOR) is determined by the pair of detectors. The spatial coordinates of the two detectors were recorded in mm from the center of the scanner FOV, and the center of each event's LOR, (X_i, Y_i, Z_i), was determined. The (X_i, Y_i, Z_i) for each event was averaged over a short time interval Δt, e.g., 1 second in this study, to generate raw COD traces in three directions: C_X for lateral, C_Y for anterior-posterior, and C_Z for superior-inferior directions; a sample is shown in Figure 1(A). Next, a semi-automatic motion detection algorithm was implemented based on the assumption that sharp changes in COD represent head motions. The detection algorithm included four phases: a) selection of the COD direction to use for motion detection, b) automatic detection of step

motions, c) visual assessment of the COD trace to identify additional motions, and d) detection of slow motions (see Discussion for details of the parameter settings in the algorithm).

a) The variance of each COD directional value was calculated from the period beginning 2 min post-injection until the end of the scan. The direction with the highest variance was chosen for motion detection (denoted $C(t)$). An example is shown in Figure 1, where C_Z contained the largest variance.

b) In the automatic detection phase, the algorithm includes: 1) applying a 1-D 15-sec median filter to obtain a new trace $M(t)$; 2) to determine motion time points (t_i, times when motion occurs), we calculate the forward difference of $M(t)$ (example shown in Supplemental Figure 1(A)) as: $D(t) = M(t+\Delta t)-M(t)$, and compare $D(t)$ with a user-defined threshold (see Discussion). If $D(t)$ exceeds the threshold, time t is chosen as a motion time point and added to a list t_i ; 3) label each frame between t_i and t_{i+1} as a "motion-free" frame (MFF); and 4) if a MFF is shorter than 30 seconds, data within this frame was excluded from further analysis. This step ensures that the preserved MFFs contain sufficient counting statistics for later motion estimation.

c) Since we only considered forward differences, i.e., an abrupt change in COD over $\Delta t = 1$ sec in phase (b), we may miss motions that were relatively slow, e.g., lasting 2-3 sec. For those obvious missed motions, we manually added t_i values based on the visual observation of the COD changes. An example can be found in Figure 1(B).

d) Some subjects exhibited slow motions, in which case a t_i value was automatically added in the middle of each MFF that was longer than 10 min (see Discussion).

Due to rapid tracer distribution changes immediately after injection, COD alters rapidly, so it is challenging for the proposed method to detect motion within very early frames, e.g., the first 2 minutes post-injection (Figure 1). Thus, we did not attempt to detect motion during the first 2 min of each study.

An example of detection results is shown in Figure 1(B). The horizontal lines at the top of the graph define each MFF and the blue vertical lines indicate the automatically-detected t_i values. Gaps in the horizontal lines at the top indicate discarded frames due to rapid motion. Green edges show the manually added t_i values in phase (c). As reference, Supplemental Figure 1(B) shows the averaged distance of the eight vertices of the reference cube (*13*) in Z direction in comparison to the position during the transmission scan, computed from the Vicra information.

Once the t_i values were determined, motions between MFFs were estimated and corrected as follows: 1) reconstruct each MFF using OSEM without attenuation correction; 2) smooth each MFF reconstruction using a 3x3x3 median filter followed by a 5-mm FWHM Gaussian filter; 3) register each MFF image to a reference frame rigidly, i.e., the first 2 min; 4) build a motion file for the entire study using each t_i and the transformation matrix to be used for all the events between t_i and t_{i+1}; 5) use MOLAR (*12*) to perform event-by-event motion compensated OSEM reconstruction (2 iteration ×30 subsets), based on the chosen frame timing. Note that for the COD method, no change in position is assumed during each MFF, however, there may be multiple MFFs within each reconstructed frame, so a final reconstructed frame may include data from multiple "poses". In addition, if any of the discarded frame periods from detection phase b) overlap with each reconstructed frame, that portion of list mode data was not included in the reconstruction of that frame. Therefore, COD results may be slightly noisier than other methods due to the discarded data.

Between-frame registrations were performed using FLIRT (*18*) with normalized mutual information as the similarity metric. Motion between the transmission and emission scans was corrected through manual registration between the MFF reference frame (without attenuation correction) and the transmission image. This transformation was incorporated into the motion file (step 4, above).

Motion correction methods for comparison

In this study, the COD-based method was compared with conventional FIR and Vicra-based event-by-event correction (referred to as Vicra), which was treated as the gold standard. For the FIR method, predefined dynamic frames (10×30sec and 17×5min) were first reconstructed using OSEM (2 iterations × 30 subsets) and registered to a reference frame, i.e., first 10 min. For the Vicra method, subject motion was recorded with a Vicra optical tracking system at 20 Hz, i.e., a rigid transformation matrix was determined every 50 msec, which was used for MC in the MOLAR reconstruction (*12*). Thus, all 3 methods used the same reconstruction pipeline with the same frame timing, just with different motion information, i.e., none for FIR, 20 Hz for Vicra, and piecewise constant (during each MFF) with possible gaps for COD. For Vicra, mean position information during the transmission scan was used for correction between emission and attenuation images. For FIR, no motion correction (NMC) was performed between emission and attenuation images, consistent with typical practice.

Image Analysis

Twelve gray matter (GM) ROIs (*17*) were used to generate time-activity curves (TACs): amygdala, caudate, cerebellum cortex, frontal, hippocampus, insula, occipital, pallidum, parietal, putamen, temporal and thalamus. The proposed COD-based approach was compared to NMC, FIR, and Vicra, which was considered as the gold standard. Mean and standard deviation of the standardized uptake value (SUV) of 0-10 min and 60-90 min frames were computed for all GM ROIs. For this comparison, for each approach, the MR was registered to each frame, i.e., 0-10 min and 60-90 min. For both ^{18}F-FDG and ^{11}C-UCB-J, tracer concentrations are higher in GM than in white matter, so SUV will typically decrease in GM if motion is present during the frame and attenuation correction (AC) mismatch is not considered. Note that the effects of AC mismatch can be very complicated depending on the motion direction and tracer distributions. In other words, a better motion correction method shall, in general, yield higher GM concentrations, unless large motion introduces inter-GM ROI cross talk.

Dynamic analysis was also performed, and the effects of residual motion were determined by its effect on fits to respective kinetic models. For both tracers, time activity curves (TACs; 27 frames: 10×30sec, 17×5min), of each ROI were computed for each correction method.

For ^{18}F-FDG, Patlak analysis was performed (*19*), with t^* set to 60 min and a 30-min scan duration was used. The slope K_i was calculated for each GM ROI. A population-based input function (PBIF) was used. To generate the PBIF, arterial plasma curves (in SUV units) from 40 subjects (not included in this study) were averaged. The PBIF was scaled for each subject using the injected dose normalized by body weight.

For ^{11}C-UCB-J, one-tissue compartment model (*20*) fitting was applied to each ROI to generate distribution volume, V_T, the tissue to plasma concentration ratio at equilibrium reflecting specific plus nonspecific binding. The rate of entry of tracer from blood to tissue, K_1, was also estimated. Note that K_1 is mostly governed by the early tracer kinetics while V_T is more affected by the late kinetics. Thus, K_1 is more sensitive to head motion in the early frames while V_T is affected more by late-frame motions. Metabolite-corrected arterial plasma curves were used as the input function.

The estimated kinetic parameters were compared between methods, using Vicra as the gold standard. In addition, the model fitting normalized residual error was calculated for each ROI, as follows:

$$\text{Residual Error} = 100\% \sqrt{\frac{\sum_i w_i \left(C_{\mathrm{T}}(t_i) - C_{\mathrm{TF}}(t_i)\right)^2}{\sum_i w_i C_{\mathrm{T}}^2(t_i)}},$$

where i is the frame number index, $C_{\mathrm{T}}(t_i)$ represents the mean ROI concentration of frame i, $C_{\mathrm{TF}}(t_i)$ is the mean concentration value of the fitted kinetic model of frame i, and w_i is the weighting factor used in the model fit. Uncorrected motion will cause increased residual error. Note that two ^{11}C-UCB-J studies underwent levetiracetam displacement at 60min, which were excluded from K_1, V_{T} and residual error calculations.

RESULTS

COD computation time (mean ± standard deviation) was 9.3±5.1 min using a single-core 2.4G Hz CPU. C_{X} was selected for automatic detection in 7 cases and C_{Z} was selected for the other 16 cases. The user-defined threshold in step (2) of phase (a) was 0.13±0.03 mm (note that COD units do not correspond to actual distances) for ^{18}F-FDG and 0.23±0.12mm for ^{11}C-UCB-J. The larger threshold variation for ^{11}C-UCB-J was due to greater variability in injected dose (^{11}C-UCB-J: 363±178 MBq; ^{18}F-FDG: 184±4 MBq). During the 90-min scans, for ^{18}F-FDG, there were 27±7 MFFs (41±14 for ^{11}C-UCB-J) which included 6.6±3.7 manually-added MFFs (8.0±3.8 for ^{11}C-UCB-J). The fraction of scan time that was discarded was 6.4±3.5% for ^{18}F-FDG (7.1±5.5% for ^{11}C-UCB-J).

In Figure 2 (^{18}F-FDG), transverse 60-90 min SUV images from three cases are shown. A coronal view of these studies is shown in Supplemental Figure 2. In terms of mean SUV compared with Vicra, the three cases yielded +3.0% (ranked 2/13, second best), +0.6% (6/13) and -2.7% (13/13) for the COD method. Visually, COD and Vicra yielded very similar images for all three cases. Detailed SUV results are shown in Supplemental Table 1. For the first 10 min, minimal SUV bias was observed among all methods, which indicates minimal motions happened during the early scan. For the 60-90 min studies, NMC yielded large negative bias (-15.7%) in SUV while FIR largely reduced the bias to -4.7% across all subjects and regions. The bias was calculated by averaging the percent difference between a given method's ROI results, e.g., NMC, and the Vicra across all the subjects, and these values were then averaged over all the ROIs. The COD method yielded positive bias for 9/12 ROIs with mean 1% higher than the Vicra, which indicated that excellent correction performance was achieved by COD. Furthermore, the ROI-level mean of inter-subject variation (with respect to Vicra) was smallest for COD (3.2%) compared with FIR (6.9%) and NMC (12.2%).

TACs of three representative ROIs, i.e., frontal (large in size), thalamus (medium) and hippocampus (small), of the selected cases are shown in Figure 3, respectively. For the first 10 min, TACs of all methods highly overlapped, which indicated minimal motions occurred, consistent with the numerical results in supplemental Table 1. For all regions, FIR (green), though outperforming NMC (red), yielded "noisier" and lower-in-value TACs for most frames as compared with the Vicra (purple). COD (blue) yielded highly overlapped TACs with Vicra for the first two subjects. For the frontal region of the first subject, COD even exceeded Vicra. For the third case in which COD performed worst, COD was slightly worse than Vicra and similar to FIR for the last 30 min.

In Figure 4 (^{11}C-UCB-J), 60-90 min transverse SUV images of three cases are shown, ranking 2/10, 4/10 and 9/10 in the COD method in terms of mean SUV bias compared to Vicra. A coronal view of these studies is shown in Supplemental Figure 3. Visually, compared to NMC, FIR substantially improved image sharpness for all cases. For the third case, the NMC image shows the large head motion for this subject, which was corrected by FIR. COD further improved sharpness and quantitation for all cases. As compared with the Vicra, COD yielded sharper and higher concentration values for the first and second cases, as can be seen in cortical regions (arrows). Note that for the Vicra method, the reflecting marker occasionally fails to maintain a rigid attachment to the subject's head, which may explain the sub-optimal performance of the Vicra in these cases (see Discussion). Detailed SUV results are provided in supplemental Table 2. For the first 10 min, COD (-1.5%) slightly outperformed FIR (-3.4%) in terms of SUV bias compared with Vicra. For 60-90min, FIR (-6.2%) yielded substantial improvement compared to NMC (-20.5%), whereas COD exceeded Vicra by 3.7%. Inter-subject standard deviation was smallest in COD (5.4%) compared with FIR (11.0%) and NMC (15.8%).

In Figure 5, TACs of the frontal, thalamus, and hippocampus regions of the three selected cases in ^{11}C-UCB-J studies are shown. Consistent with the visual comparison shown in Figure 4, COD outperformed Vicra by yielding higher TACs in value for the first and second cases while comparable for the third case. Note that bolus injection only was used for the first two cases while bolus plus infusion was used for the third.

For ^{18}F-FDG dynamic studies, K_i results are shown in Table 1. NMC yielded a large negative bias (-18%) with very high inter-subject variation (39%) compared with Vicra. FIR substantially reduced the bias and inter-subject variation to -2.6±19.8%. The COD method outperformed FIR with +3.6% mean bias and 10.9% inter-subject SD. In terms of residual error of Patlak fitting, averaging over all regions and subjects, NMC yielded 4.6%, FIR reduced the

error by half (2.6%) whereas COD yielded better performance, comparable to Vicra, 1.5% vs. 1.2%, respectively. Residual error results are shown in Supplemental Table 3.

For ^{11}C-UCB-J dynamic studies, K_1 and V_T results are shown in Table 2. For all methods, very small K_1 bias was found since K_1 is sensitive to motion in the early frames, but there was minimal motion from 0-10min (Supplemental Table 2). Note that COD yielded the lowest inter-subject variation (1.9%) compared with FIR (6.2%) and NMC (9.0%). For V_T, NMC yielded large negative bias and inter-subject variation (-20.0±12.5%) whereas FIR showed great improvement in both (-5.3±9.4%). COD yielded higher V_T values (3.7±5.2%) than Vicra. Since COD yielded higher activity values than Vicra in SUV analysis (Supplemental Table 2), V_T estimated using COD will be higher, and are likely to be closer to the truth. In terms of model fitting residual error, COD (2.5%) outperformed all other approaches, i.e., NMC (7.3%), FIR (4.6%) and Vicra (2.8%) (Supplemental Table 4). Therefore, COD yielded the best performance in MC for the ^{11}C-UCB-J studies.

DISCUSSION

In this study, we proposed a data-driven head motion detection method followed by rigid MC. The proposed method was compared with frame-based image registration method and hardware-based event-by-event Vicra method, which was treated as the gold standard. For ^{18}F-FDG and ^{11}C-UCB-J, the proposed method outperformed FIR and achieved comparable or better results to Vicra for both static and dynamic data.

In theory, the Vicra method should yield the best possible performance. However, we found that COD yielded slightly higher gray matter SUVs (1% for ^{18}F-FDG, 3.7% for ^{11}C-UCB-J), suggesting that Vicra HMT was not ideal for this patient cohort with large head motion. Ideally, the Vicra tool must be rigidly fixed to the head, but this may fail in several ways. For instance, the tool may permanently displace from its original location due to imperfect fixation. In this study, although we excluded scans containing obvious Vicra failure based on the technologist report, the positive percent difference of COD over Vicra indicated that imperfect Vicra HMT still existed. Thus, the excellent performance by COD showed that a data-driven approach can be as effective as HMT.

In this study, the COD method discarded ~7% of the counts, due to excessive and frequent motion. In contrast, Vicra used all the data. If these large-motion periods affect the Vicra tracking, e.g., by introducing non-rigid attachment between the marker and subject's head, then by excluding the same data, the performance of Vicra may

improve. If so, a hybrid approach, i.e., Vicra plus COD, could be implemented in the future to further improve Vicra tracking.

As an alternative to all the aforementioned approaches, markerless motion tracking using camera systems requires no attachment to a patient (*21*). However, the accuracy of such methods remain to be thoroughly tested, since the results can be affected by non-rigid facial expression changes (*21*) and performance may vary for different populations.

Success of the proposed method can be tracer dependent. Here, we used ^{11}C-UCB-J and ^{18}F-FDG for the following reasons: ^{18}F-FDG is the most clinically used PET tracer while ^{11}C-UCB-J, as a very novel tracer, has shown its efficacy for studying multiple neurological disorders (*16,22*), and has great potential for wider clinical and research use. In addition, the 20-min half-life of ^{11}C added a challenge for the COD algorithm due to the high-noise condition for the late scan frames. However, we note that both tracers have a broad distribution in the brain with patterns that do not vary substantially over time. This characteristic could make the image registration step more robust than for tracers with those with heterogeneous and time-varying distribution, e.g., ^{11}C-Raclopride. In the future, we will evaluate COD with a wider variety of tracers.

In this implementation of the algorithm, several user-defined parameters were applied: the length of the median filter applied to the COD trace, the threshold for motion determination, the minimum duration of a MFF, the 5-min maximum length of a MFF for slow-motion detection, and the smoothing kernel for MFF reconstructions. These parameters were chosen empirically. Here, we clarify the rationale behind the choice of parameters for this algorithm: 5-min maximum MFF length was chosen as a tradeoff among the sensitivity to slow motion, the computational cost, and the registration accuracy which is affected by noise and tracer distribution change. The 30-sec shortest MFF was chosen to be the same length as the shortest dynamic frame. Another choice could be a count-level based approach, in which the threshold could be set based on the minimal number of counts for each MFF. The 15-sec median filter and threshold were tested against human detection of the abrupt changes in the COD curve for the same studies, and we adjusted the threshold to best match the human observations. In addition, in this study, we did not evaluate how much of the good performance of the COD method was due to manually added MFFs. In the future, further optimization of each parameter is required.

There are other limitations of this study. First, the COD method cannot accurately detect motion in the early period postinjection, due to rapid changes in tracer distribution, so data-driven MC during this period will remain challenging. Also, here we used list-mode reconstruction, however, our approach can be extended to sinogram-based reconstruction (*23*) with minimal modification. In addition, we compared the COD-based approach to conventional FIR, in which each frame was reconstructed with attenuation correction. Thus, FIR not only suffered from intra-frame motion, but also attenuation mismatch artifact. To minimize the latter effect, motion estimation could be performed using images without attenuation correction (*13,24*) . We note that in this study, we did not compare our approach to other data-driven approaches (*3-5*); such a comparison is important to clarify what method will provide the most robust and accurate method for motion detection and correction. The current detection method may detect some false-positive motions (in the absence of motion) purely due to noise in the COD. However, such false-positive detected motion should not substantially affect the reconstruction results despite of the fact that small errors may still occur since the registration is subject to image noise. In addition, false-positive detection could also occur due to very rapid tracer kinetics.

CONCLUSION

We proposed a data-driven head motion detection method followed by rigid motion correction. The proposed method was compared with frame-based image registration method and the hardware-based Vicra method. For both ^{18}F-FDG and ^{11}C-UCB-J, the proposed method outperformed FIR and achieved comparable or better results compared with Vicra for both static and dynamic studies.

ACKNOWLEGEMENT

This work was funded by NIH grants R01AG052560, R01NS094253 and R03EB027209. This publication was made possible by CTSA Grant Number UL1 TR000142 from the National Center for Advancing Translational Science (NCATS), a component of the National Institutes of Health (NIH). Its contents are solely the responsibility of the authors and do not necessarily represent the official view of NIH.

KEY POINTS

QUESTION: Can data-driven head motion correction method achieve similar performance as compared to hardware-based motion tracking?

PERTINENT FINDINGS: In a dynamic PET study of subjects with large head motions using ^{18}F-FDG (N=13) or ^{11}C-UCB-J (N=10), both static and dynamic measures showed that the proposed data-driven head motion detection and correction method yielded comparable or better results as compared with the hardware-based approach.

IMPLICATIONS FOR PATIENT CARE: Data-driven head motion correction can be reliably performed for clinical or research brain PET scans for tracers with broad distributions.

REFERENCES

1. Costes N, Dagher A, Larcher K, Evans AC, Collins DL, Reilhac A. Motion correction of multi-frame PET data in neuroreceptor mapping: simulation based validation. *Neuroimage.* 2009;47:1496-1505.

2. Picard Y, Thompson CJ. Motion correction of PET images using multiple acquisition frames. *Ieee Transactions on Medical Imaging.* 1997;16:137-144.

3. Thielemans K, Schleyer P, Dunn J, Marsden PK, Manjeshwar RM. Using PCA to detect head motion from PET list mode data. *2013 Ieee Nuclear Science Symposium and Medical Imaging Conference (Nss/Mic).* 2013.

4. Huang C, Petibon Y, Normandin M, Li Q, El Fakhri G, Ouyang J. Fast head motion detection using PET list-mode data. *Journal of Nuclear Medicine.* 2015;56:1827-1827.

5. Feng T, Yang D, Zhu W, Dong Y, Li H. Real-time data-driven rigid motion detection and correction for brain scan with listmode PET. Paper presented at: 2016 IEEE Nuclear Science Symposium, Medical Imaging Conference and Room-Temperature Semiconductor Detector Workshop (NSS/MIC/RTSD); 29 Oct.-6 Nov. 2016, 2016.

6. Schleyer PJ, Dunn JT, Reeves S, Brownings S, Marsden PK, Thielemans K. Detecting and estimating head motion in brain PET acquisitions using raw time-of-flight PET data. *Phys Med Biol.* 2015;60:6441-6458.

7. Rahmim A, Rousset O, Zaidi H. Strategies for Motion Tracking and Correction in PET. *PET Clinics.* 2007;2:251-266.

8. Gallezot J, Lu Y, Naganawa M, Carson RE. Parametric Imaging with PET and SPECT. *IEEE Transactions on Radiation and Plasma Medical Sciences.* 2019:1-1.

9. Markiewicz PJ, Thielemans K, Schott JM, et al. Rapid processing of PET list-mode data for efficient uncertainty estimation and data analysis. *Phys Med Biol.* 2016;61:N322-336.

10. Ren S, Jin X, Chan C, et al. Data-driven event-by-event respiratory motion correction using TOF PET list-mode centroid of distribution. *Physics in Medicine and Biology.* 2017;62:4741-4755.

11. Lu Y, Gallezot JD, Naganawa M, et al. Data-driven voluntary body motion detection and non-rigid event-by-event correction for static and dynamic PET. *Phys Med Biol.* 2019;64:065002.

12. Carson RE, Barker CW, Liow J-S, Johnson CA. Design of a motion-compensation OSEM list-mode algorithm for resolution-recovery reconstruction for the HRRT. Paper presented at: Design of a motion-compensation OSEM list-mode algorithm for resolution-recovery reconstruction for the HRRT, 2003.

13. Jin X, Mulnix T, Gallezot JD, Carson RE. Evaluation of motion correction methods in human brain PET imaging--a simulation study based on human motion data. *Med Phys.* 2013;40:102503.

14. Dinelle K, Blinder S, Cheng J, et al. Investigation of Subject Motion Encountered During a Typical Positron Emission Tomography Scan. Paper presented at: 2006 IEEE Nuclear Science Symposium Conference Record; 29 Oct.-1 Nov. 2006, 2006.

15. Finnema SJ, Nabulsi NB, Eid T, et al. Imaging synaptic density in the living human brain. *Science Translational Medicine.* 2016;8:348ra396-348ra396.

16. Chen MK, Mecca AP, Naganawa M, et al. Assessing Synaptic Density in Alzheimer Disease With Synaptic Vesicle Glycoprotein 2A Positron Emission Tomographic Imaging. *JAMA Neurol.* 2018.

17. Greve DN, Salat DH, Bowen SL, et al. Different partial volume correction methods lead to different conclusions: An (18)F-FDG-PET study of aging. *Neuroimage.* 2016;132:334-343.

18. Jenkinson M, Smith S. A global optimisation method for robust affine registration of brain images. *Med Image Anal.* 2001;5:143-156.

19. Patlak CS, Blasberg RG, Fenstermacher JD. Graphical evaluation of blood-to-brain transfer constants from multiple-time uptake data. *J Cereb Blood Flow Metab.* 1983;3:1-7.

20. Finnema SJ, Nabulsi NB, Mercier J, et al. Kinetic evaluation and test-retest reproducibility of [(11)C]UCB-J, a novel radioligand for positron emission tomography imaging of synaptic vesicle glycoprotein 2A in humans. *J Cereb Blood Flow Metab.* 2017:271678X17724947.

21. Kyme AZ, Se S, Meikle SR, Fulton RR. Markerless motion estimation for motion-compensated clinical brain imaging. *Phys Med Biol.* 2018;63:105018.

22. Holmes SE, Scheinost D, Finnema SJ, et al. Lower synaptic density is associated with depression severity and network alterations. *Nature Communications.* 2019;10.

23. Reilhac A, Merida I, Irace Z, et al. Development and validation of a rebinner with rigid motion correction for the Siemens PET-MR scanner: Application to a large cohort of [11C]-PIB scans. *Journal of Nuclear Medicine.* 2018.

24. Ye H, Wong KP, Wardak M, et al. Automated movement correction for dynamic PET/CT images: evaluation with phantom and patient data. *PLoS One.* 2014;9:e103745.

Table 1. ^{18}F-FDG K_i difference (%) compared to Vicra.

	No Motion Correction (NMC)	Frame-based Image Registration (FIR)	Centroid of Distribution (COD)
Amygdala	18.0±60.4	-5.8±22.4	3.1±11.3
Caudate	-11.3±39.0	-0.8±29.8	6.3±18.2
Cerebellum	-21.9±38.2	-2.1±12.4	2.6±9.8
Frontal	-36.0±43.4	-2.6±25.4	8.5±12.0
Hippocampus	-4.3±40.9	-5.6±19.7	-2.5±13.3
Insula	-11.7±19.3	-3.9±14.1	4.7±8.1
Occipital	-19.3±27.5	3.4±19.7	7.5±11.8
Pallidum	-9.4±47.6	0.2±15.2	0.9±12.9
Parietal	-27.6±40.9	-1.4±19.3	3.6±8.6
Putamen	-35.0±48.3	-1.3±23.9	6.0±9.7
Temporal	-27.5±27.6	-3.6±16.4	3.9±7.4
Thalamus	-30.3±38.0	-8.4±19.0	-0.9±7.3
Average difference (%)	-18.0	-2.6	3.6
Average SD (%)	39.2	19.8	10.9

(SD: standard deviation across all subjects)

Table 2. ^{11}C-UCB-J K_1 and V_T difference (%) compared to Vicra.

	No Motion Correction (NMC)		Frame-based Image Registration (FIR)		Centroid of Distribution (COD)	
Parameter	K_1	V_T	K_1	V_T	K_1	V_T
Amygdala	0.8±10.4	-24.6±13.0	-1.2±7.6	-7.5±12.5	-0.7±2.7	5.0±6.2
Caudate	-3.5±11.3	-29.9±12.6	-3.9±7.2	-6.6±8.6	-0.8±2.0	5.4±5.3
Cerebellum	0.0±5.5	-10.4±9.9	-0.8±3.6	-4.6±6.8	-0.4±1.5	2.1±4.4
Frontal	1.2±12.8	-37.8±12.9	-3.1±8.0	-5.2±8.7	0.3±1.1	3.5±2.9
Hippocampus	-4.3±6.7	-14.0±12.9	-1.5±6.5	-6.1±10.2	0.5±2.2	3.6±5.7
Insula	2.1±9.4	-21.1±11.5	-0.7±5.4	-6.7±7.5	0.4±0.7	2.1±3.5
Occipital	0.3±6.8	-10.5±12.8	-0.3±4.5	-0.6±10.9	-0.9±2.5	6.2±7.5
Pallidum	-0.7±6.4	7.7±19.3	-0.2±7.1	-5.1±10.5	0.4±3.2	0.5±7.0
Parietal	0.2±10.5	-25.8±10.3	-1.6±6.5	-1.3±11.2	-0.8±2.4	5.5±6.2
Putamen	1.3±8.5	-29.9±9.7	-1.2±5.2	-7.8±7.3	0.2±1.1	2.5±4.2
Temporal	0.8±10.9	-27.2±10.9	-1.1±6.2	-5.6±12.7	-0.1±1.8	5.8±5.6
Thalamus	-2.4±8.7	-16.7±14.8	-2.2±6.3	-6.0±5.6	-0.6±1.7	2.4±4.2
Average difference (%)	-0.5	-20.0	-1.5	-5.3	-0.2	3.7
Average SD (%)	9.0	12.5	6.2	9.4	1.9	5.2

(SD: standard deviation across subjects)

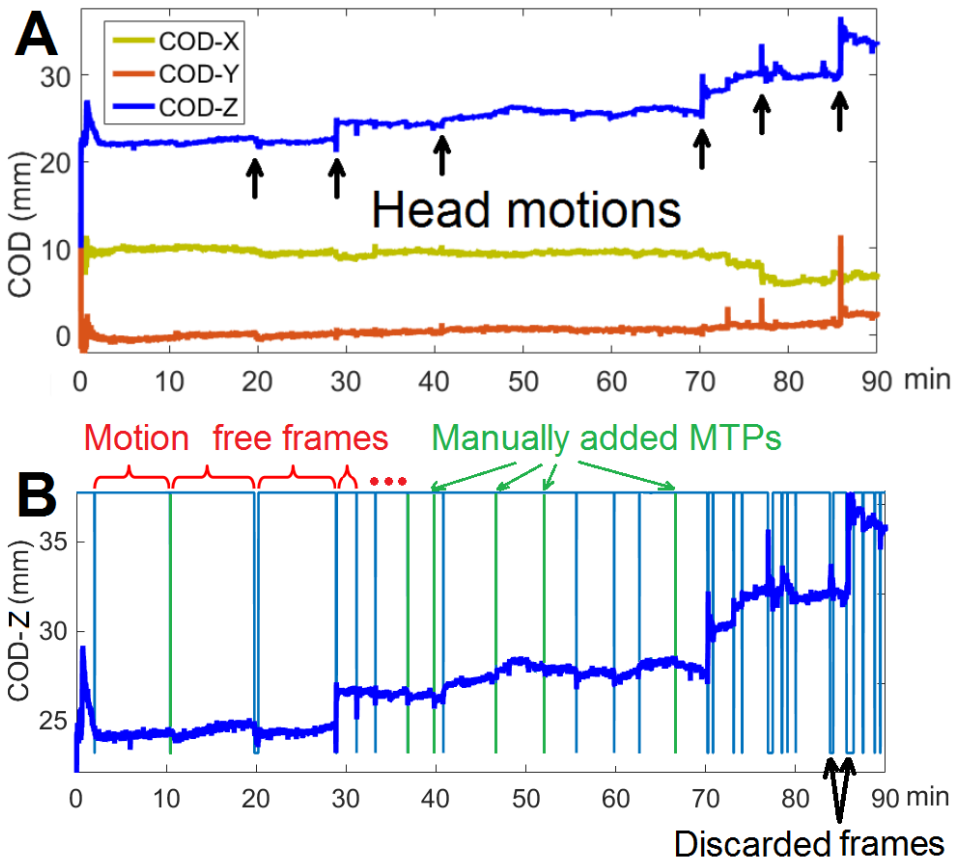

Figure 1 (A) Centroid Of Distribution (COD) traces in three directions of an ^{18}F-FDG study. Arrows denote abrupt changes in C_Z, which indicate head motions. (B) Motion detection results. Blue vertical edges indicate motion time points (MTP) from automated detection and green vertical edges indicate manually-added points from visual assessment of undetected abrupt changes. Top horizontal line segments indicate a preserved motion-free frame and short bottom line segments indicate discarded frames due to overly-frequent motion.

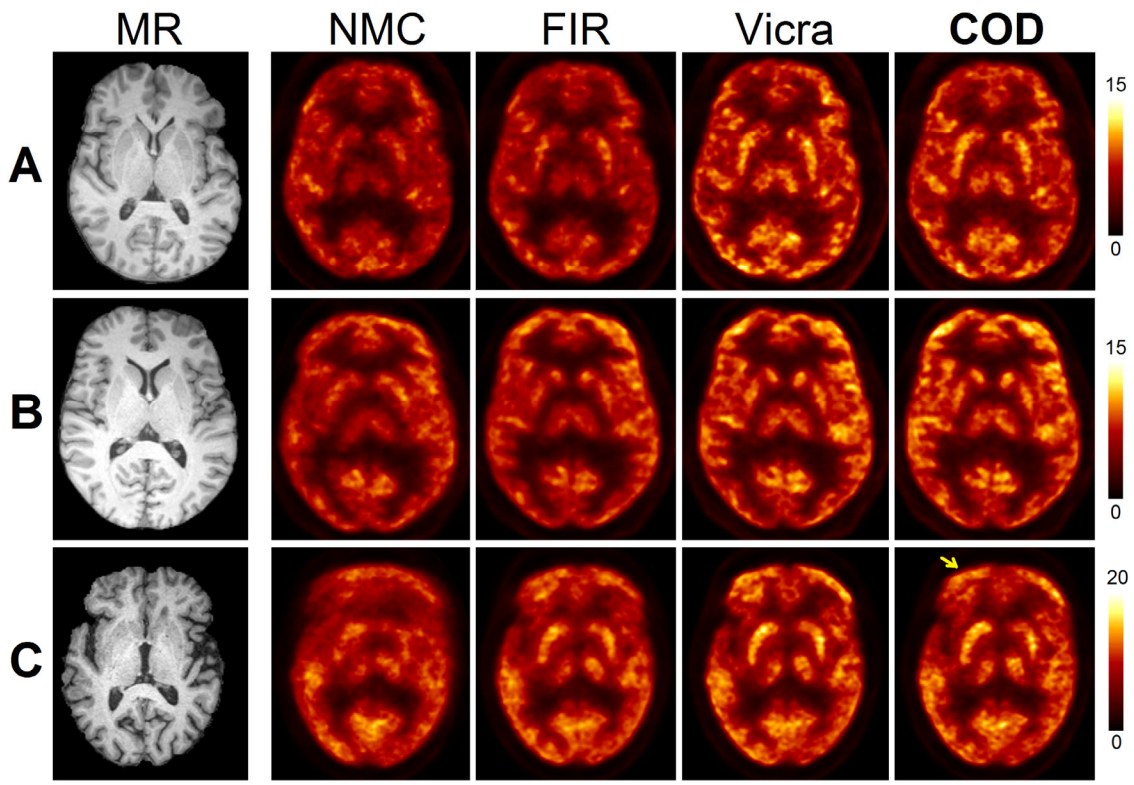

Figure 2. Sample slices in SUV units of motion-corrected reconstructions of ^{18}F-FDG studies (60-90min). Studies from (A), (B) and (C) ranked 2/13, 6/13 and 13/13 (worst) of the COD-based approach, respectively. Subtle motion blur at frontal region (arrow) can be seen in COD (C).

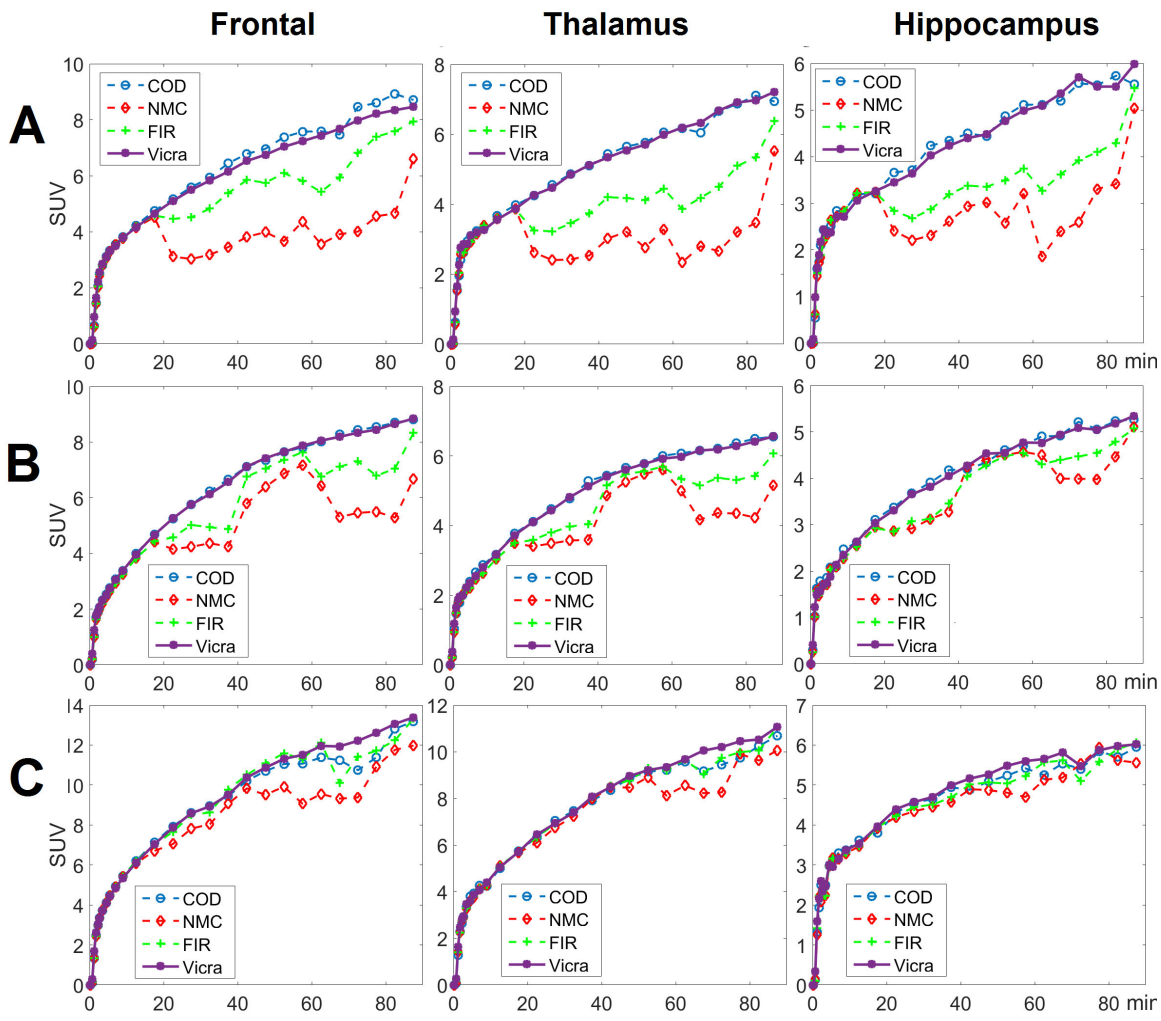

Figure 3. Three time activity curve examples of the ^{18}F-FDG studies for three regions (columns). Studies from (A), (B) and (C) ranked 2/13, 6/13 and 13/13 (worst) of the COD-based approach, respectively.

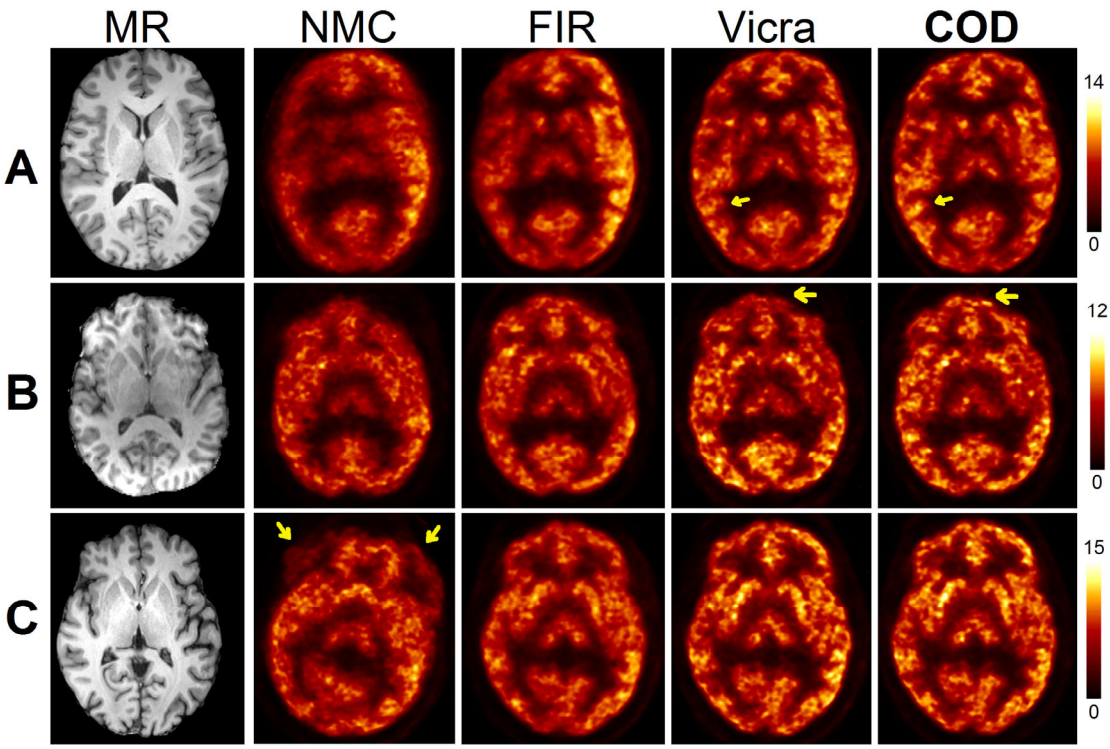

Figure 4. Sample slices in SUV units of motion-corrected reconstructions of ^{11}C-UCB-J studies (60-90min). Studies from (A), (B) and (C) ranked 2/10, 4/10 and 9/10 of the COD-based approach, respectively. Arrows in (A) and (B) point to cortical regions, where COD showed sharper and higher concentration values than Vicra. Arrows in (C) show the large magnitude of head motion in this subject.

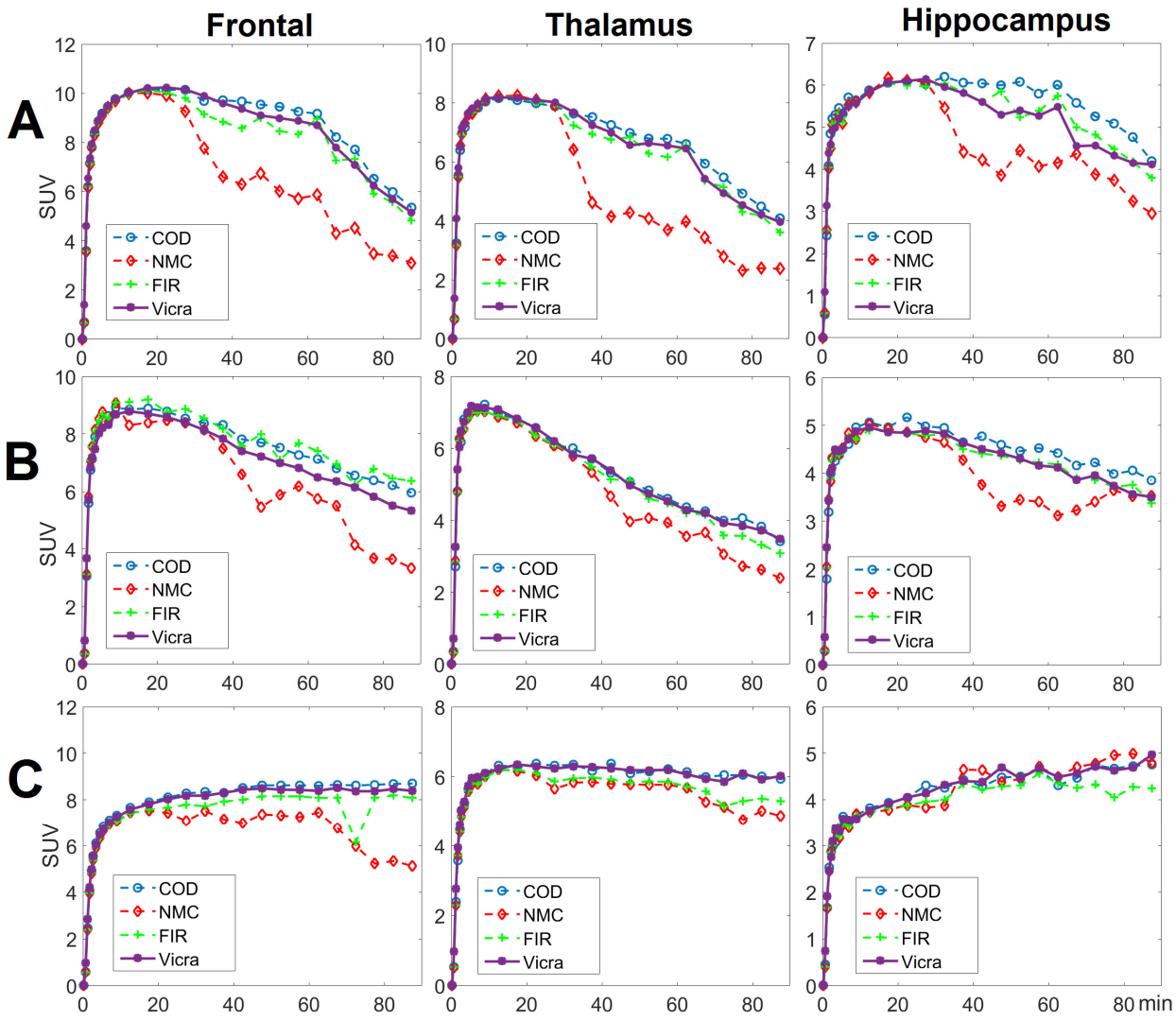

Figure 5. Three time activity curve examples of the ^{11}C-UCB-J studies for three regions (columns). Studies from (A), (B) and (C) ranked 2/10, 4/10 and 9/10 of the COD-based approach, respectively. Case A used bolus injection and underwent displacement at 60 min. Case B used bolus injection while C used an infusion paradigm.

Supplemental material

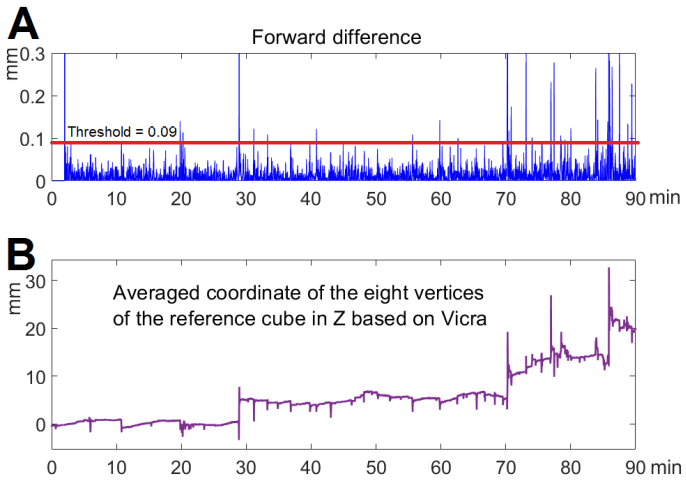

SUPPLEMENTAL FIGURE 1. (A) Forward difference of Figure 1(B) used in automatic MTP detection with the motion threshold set to 0.09. (D) Averaged coordinates absolute distance of the eight vertices of the reference cube in Z direction, which were computed based on the Vicra motion information.

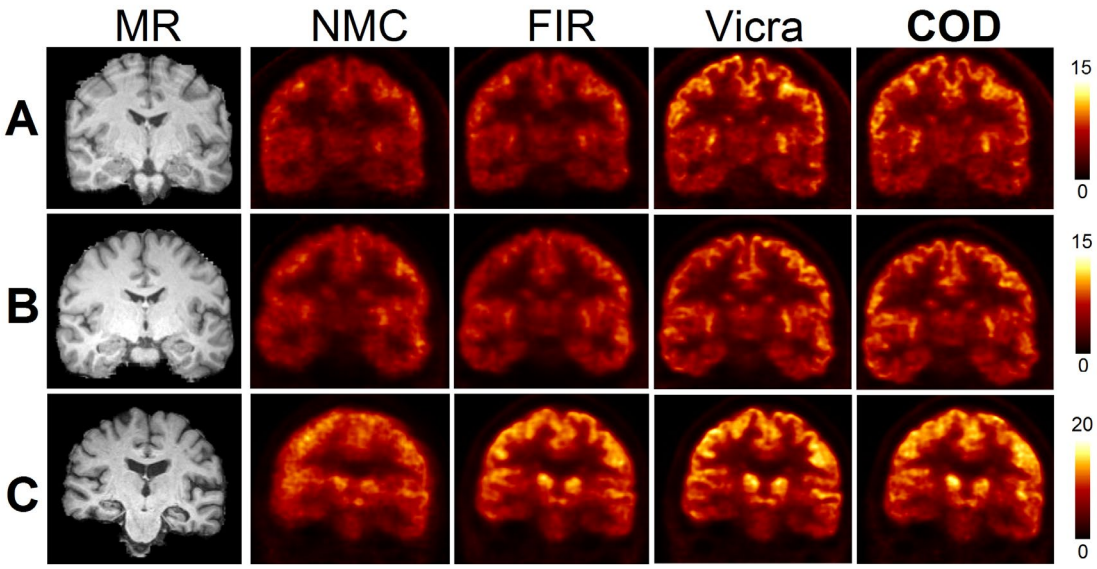

SUPPLEMENTAL FIGURE 2. Same as Figure 2 in coronal orientation.

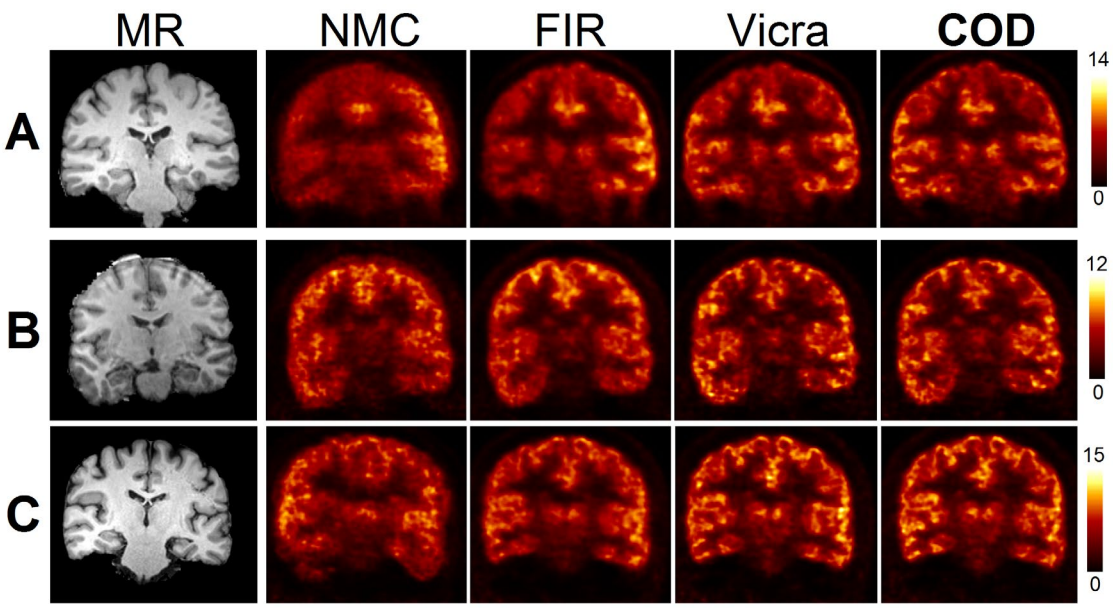

SUPPLEMENTAL FIGURE 3. Same as Figure 4 in coronal orientation.

Supplemental Table 1. ^{18}F-FDG SUV difference (%) compared to Vicra.

	No Motion Correction (NMC)		Frame-based Image Registration (FIR)		Centroid of Distribution (COD)	
Time(min)	0-10	60-90	0-10	60-90	0-10	60-90
Amygdala	-1.9±3.6	-9.7±13.3	-1.5±3.5	-5.7±7.0	-2.9±4.1	1.8±2.6
Caudate	-3.7±4.0	-22.8±10.0	-3.2±3.4	-6.5±8.7	-2.4±3.7	-2.6±4.6
Cerebellum	-2.4±1.7	-14.6±16.1	-2.3±1.7	-5.4±6.0	-2.8±2.4	0.8±2.4
Frontal	-3.8±3.0	-25.3±9.9	-3.3±2.3	-4.0±6.6	-2.2±2.7	0.2±3.4
Hippocampus	-2.0±1.6	-11.4±10.6	-1.7±1.5	-6.0±6.8	-2.2±4.9	-1.8±1.8
Insula	-2.2±2.2	-10.7±11.1	-2.3±2.0	-4.1±5.4	-1.3±2.9	1.6±1.8
Occipital	-2.9±2.6	-12.1±9.9	-2.9±2.2	-2.1±7.6	-2.4±2.4	4.7±6.9
Pallidum	-1.5±2.9	-0.7±17.4	-1.9±2.9	-2.3±7.2	-2.6±3.5	4.8±3.2
Parietal	-3.4±2.6	-17.7±11.4	-3.1±2.2	-4.7±7.3	-2.8±2.6	0.4±4.1
Putamen	-3.9±3.1	-22.5±11.8	-3.6±2.8	-4.4±5.7	-3.3±3.2	1.7±2.9
Temporal	-3.1±2.0	-22.0±12.8	-2.9±1.8	-4.8±5.9	-2.7±2.5	0.9±2.6
Thalamus	-2.3±2.4	-18.5±12.7	-2.1±2.3	-6.5±7.9	-2.5±3.5	-0.5±1.8
Average difference (%)	-2.8	-15.7	-2.6	-4.7	-2.5	1.0
Average SD (%)	2.6	12.2	2.4	6.9	3.2	3.2

Mean ± standard deviation across subjects.

Supplemental Table 2. ^{11}C-UCB-J SUV difference (%) compared to Vicra.

	No Motion Correction (NMC)		Frame-based Image Registration (FIR)		Centroid of Distribution (COD)	
Time(min)	0-10	60-90	0-10	60-90	0-10	60-90
Amygdala	-2.5±4.6	-23.1±15.1	-2.4±4.1	-7.0±10.5	-0.6±1.9	4.5±5.2
Caudate	-5.0±6.9	-24.2±15.7	-4.6±5.5	-5.8±10.1	-1.3±1.3	6.4±6.3
Cerebellum	-2.8±1.5	-12.7±13.8	-2.7±1.3	-6.4±10.2	-2.0±1.4	2.6±4.7
Frontal	-4.4±7.3	-39.0±14.9	-4.0±6.2	-6.3±12.0	-0.6±1.2	3.9±3.4
Hippocampus	-3.6±5.3	-12.8±8.9	-3.5±4.8	-7.8±11.5	-0.8±1.4	1.6±6.7
Insula	-2.9±2.9	-22.4±18.2	-2.7±2.9	-7.2±8.4	-1.3±1.0	1.9±3.3
Occipital	-2.9±2.0	-14.3±15.2	-2.9±2.0	-2.3±11.7	-2.4±2.2	6.4±7.4
Pallidum	-2.5±4.6	5.9±23.0	-2.2±4.6	-4.1±12.3	-1.1±1.6	1.3±7.1
Parietal	-4.1±4.2	-28. ±15.1	-4.1±3.7	-3.5±12.7	-2.5±1.8	4.3±6.4
Putamen	-3.6±4.6	-30.2±13.9	-3.3±3.9	-7.6±8.4	-1.6±1.6	3.2±3.7
Temporal	-3.8±2.9	-27.9±17.3	-3.7±2.7	-7.4±12.4	-1.5±1.0	4.4±4.6
Thalamus	-4.4±4.8	-16.9±18.4	-4.2±4.2	-9.4±11.8	-2.0±1.5	3.7±5.5
Average difference (%)	-3.5	-20.5	-3.4	-6.2	-1.5	3.7
Average SD (%)	4.3	15.8	3.8	11.0	1.5	5.4

(SD: standard deviation across all subjects)

Supplemental Table 3. ^{18}F-FDG Patlak-model fitting residual error (averaged over subjects).

	No Motion Correction (NMC)	Frame-based Image Registration (FIR)	Vicra	Centroid of Distribution (COD)
Amygdala	4.8%	4.0%	2.6%	3.4%
Caudate	5.2%	3.8%	1.4%	2.3%
Cerebellum Cortex	4.2%	1.7%	0.7%	0.7%
Frontal	4.5%	3.2%	0.7%	1.6%
Hippocampus	4.2%	2.4%	1.6%	2.0%
Insula	3.6%	1.8%	0.8%	1.1%
Occipital	2.7%	1.8%	1.0%	1.0%
Pallidum	6.6%	2.4%	2.0%	1.7%
Parietal	3.3%	2.2%	0.7%	1.1%
Putamen	6.1%	2.9%	1.1%	1.4%
Temporal	4.9%	2.3%	0.8%	0.8%
Thalamus	5.2%	2.4%	1.0%	1.2%
Average	4.6%	2.6%	1.2%	1.5%

Supplemental Table 4. ^{11}C-UCB-J 1T-model fitting residual error (averaged over subjects).

	No Motion Correction (NMC)	Frame-based Image Registration (FIR)	Vicra	Centroid of Distribution (COD)
Amygdala	8.4%	6.0%	5.1%	4.2%
Caudate	11.2%	5.4%	2.8%	2.9%
Cerebellum Cortex	4.8%	3.4%	2.2%	2.1%
Frontal	9.2%	5.7%	1.5%	1.7%
Hippocampus	7.7%	5.1%	4.5%	4.1%
Insula	5.7%	3.8%	2.1%	2.1%
Occipital	5.2%	3.5%	2.2%	1.5%
Pallidum	6.1%	4.8%	3.9%	3.6%
Parietal	7.2%	4.3%	2.1%	1.5%
Putamen	7.6%	4.2%	2.1%	1.8%
Temporal	6.9%	4.3%	2.0%	1.4%
Thalamus	7.1%	4.4%	2.5%	2.5%
Average	7.3%	4.6%	2.8%	2.5%